A local finite element implementation for imposing periodic boundary conditions on composite micromechanical models

J.M. Tyrus [a], M. Gosz [a,*], E. DeSantiago [b]

[a] *Department of Mechanical, Materials, and Aerospace Engineering, Illinois Institute of Technology, 10 West 32nd Street, Chicago, IL 60616-3793, United States*
[b] *Department of Civil and Architectural Engineering, Illinois Institute of Technology, 10 West 32nd Street, Chicago, IL 60616-3793, United States*

Abstract

Recent advances in computational speed have resulted in the ability to model composite materials using larger representative volume elements (RVEs) with greater numbers of inclusions than have been previously studied. Imposing periodic boundary conditions on very large RVEs can mean enforcing thousands of constraint equations. In addition, a periodic mesh is essential for enforcing the constraints. The present study investigates a method that uses a local implementation of the constraints that does not adversely affect the computational speed. The present study demonstrates the method for two-dimensional triangular and square RVEs of periodically-spaced regular hexagonal and square arrays of composite material containing fibers of equal radii. To impose the boundary conditions along the edges, this study utilizes a cubic interpolant to model the displacement field along the matrix edges and a linear interpolant to model the field along the fiber edges. It is shown that the method eliminates the need for the conventional node-coupling scheme for imposing periodic boundary conditions, consequently reducing the number of unknowns to the interior degrees of freedom of the RVE along with a small number of global parameters. The method is demonstrated for periodic and non-periodic mesh designs.
© 2006 Elsevier Ltd. All rights reserved.

Keywords: Finite element method; Representative volume element; Periodic boundary conditions; Micromechanical modeling; Composites

1. Introduction

Recent advances in computational speed have resulted in the ability to model composite materials using larger representative volume elements (RVEs) with greater numbers of inclusions than have been previously studied for the effective evaluation of material properties, failure analysis, and constitutive law development. Hashin (1983) presents a comprehensive review of the early work done in the analysis of the properties of composite materials prior to the proliferation of computer technology. With the increase in computer resources

* Corresponding author. Fax: +1 312 567 7230.
  E-mail addresses: tyrujas@iit.edu (J.M. Tyrus), gosz@iit.edu (M. Gosz).

available, composite materials can be investigated using techniques that were formerly not viable. These techniques can be used to predict the characteristics of composite materials in order to achieve a greater understanding of the properties of these materials.

There are numerous theoretical micromechanical models that have been widely used to predict the characteristics of composite materials. An evaluation of the Differential Method, the Generalized Self Consistent Method, and the Mori-Tanaka Method is given by Christensen (1990). To test the predictions given by the micromechanical models, it is often necessary to use upper and lower bounding values for the elastic properties of composite materials. Bounds for elastic properties of composite materials have been derived by Hashin and Shtrikman (1963) using variational principles in elasticity. The bounds provide a reasonable estimate of the effective moduli. In addition to bounds for composites with perfectly bonded constituents, Hashin (1992) has also constructed bounds for two-phase materials with imperfect interfaces.

The interface of a composite material plays a large part in the effective properties of the material. The role of the interface in the strength of composite materials has been addressed in the early study of composites by Tsai and Hahn (1980). More recently, interface bond strength has been studied by Yeh (1992) through the creation of a finite-element model that allows modeling of either perfect bonding or debonding based on the state of interfacial stress, thereby illustrating that interfacial tensile strength influences the transverse properties of composites. To study interface decohesion at metal–ceramic interfaces, Needleman (1987) introduced a cohesive crack model to describe the entire process of decohesion starting from initial debonding. Decohesion was also investigated with interface models that relate tractions to displacement jumps in work performed by Corigliano (1993) to develop a numerical integration method for interface constitutive laws. The determination of mechanical properties of fiber-reinforced composites with viscoelastic interphases was investigated by Gosz et al. (1991) by studying the role of the interface on the transverse properties of the composite from both a macroscopic and microscopic perspective. A detailed review of composite interface mechanics models is presented by Liu and Mai (1999).

The modeling of interface mechanics models has been greatly enhanced through the use of the finite element method. Full numerical simulation of delamination fracture processes in polymer–matrix composites using interface models has been performed by Bianchi et al. (2006). New interface finite elements have also been recently created to model the region between the fiber and matrix. Segurado and Llorca (2004) have developed a new three-dimensional quadratic interface element consisting of two six-noded triangular surfaces that initially lie together and connect the faces of adjacent tetrahedra. The surfaces separate as the adjacent elements deform, thereby creating normal and shear stresses. In addition, Thoutireddy et al. (2002) have developed a composite tetrahedral finite element composed of twelve four-node linear tetrahedral elements with an assumed linear displacement field in each tetrahedral element. Schellekens and DeBorst (1993) provide a thorough study of the analysis of interface elements in micromechanical models.

One of the key issues that arises when creating finite element micromechanical models is the size of the RVE necessary to capture all of the prominent features of the entire body under study. Drugan and Willis (1996) state that the minimum size of the RVE is the smallest volume element of the composite that is "statistically representative of the composite". They have shown that the minimum RVE size is at least twice the diameter of the reinforcement, citing a maximum error of five percent in elastic constants obtained with this RVE size. Gusev (1997) studied disordered periodic elastic composite unit cells composed of various numbers of identical spheres in order to determine the scatter in elastic constants obtained with different numbers of spheres and found that the scatter is small with only a few dozen spheres in the cell. Three-dimensional multiparticle cubic cells were used in the studies of Eckschlager et al. (2002) and Llorca and Segurado (2004).

When homogeneous boundary conditions are applied to a macroscopic composite, the deformation in each RVE is identical and the deformation along each RVE edge is compatible. Consequently, the mechanical response of a composite material can be obtained by applying periodic boundary conditions to a single RVE. The conventional method of applying periodic boundary conditions has been to pair nodes on opposite faces of the RVE. This method has been used by Segurado and Llorca (2002) and Berger et al. (2005). In the conventional node-coupling scheme, opposite nodes on opposite boundaries of the RVE must be paired to ensure continuous deformation. For each pair of nodes with the same in-plane coordinates, the displacement components on the coupled boundaries are constrained with a constraint equation. This pairing of nodes ensures periodic deformation and compatibility on opposite sides of the RVE. Imposing the constraints on

opposite nodes according to this conventional node-coupling scheme can mean enforcing thousands of constraint equations, resulting in a very time-consuming task to impose the periodic boundary conditions on the RVE.

It has been shown by Gusev (1997), Gusev (2001) that periodic boundary conditions can be imposed without the employment of multipoint constraints. Using a periodic mesh, i.e., the mesh is structured such that a node on an outer edge has a corresponding node on the opposite outer edge, the degrees of freedom of a node on an outer edge of the RVE are set equal to the degrees of freedom of the corresponding node on the opposing edge of the mesh, thereby circumventing the need to apply multipoint constraints on the boundary degrees of freedom of the RVE. An effective strain is applied to the entire RVE by simply prescribing the displacements of the nodes at the vertices of the RVE. This method eliminates the need to apply any prescribed boundary displacements except at the vertices of the RVE. Despite its advantages, the method is limited to rectangular or cubic RVEs and requires constant strain elements for implementation. In addition, a periodic mesh is necessary to carry out the method, thereby requiring a significant effort in mesh generation.

The present study proposes a new method for implementing the constraints on a local level. By utilizing interpolants to model the displacement field along the edges of the RVE, the method eliminates the need for conventional node-coupling schemes for imposing periodic boundary conditions, consequently reducing the number of unknowns to the interior degrees of freedom of the RVE along with a finite number of global parameters. In addition, since the nodes on adjacent faces are no longer coupled, the mesh on opposite surfaces of the RVE no longer needs to be identical, resulting in greater flexibility in mesh design by allowing for analysis using non-periodic meshes. The proposed method results in a valuable computational savings that greatly simplifies the pre-processing stage of the analysis to find material properties, failure criteria, or constitutive laws for composite materials.

2. Representative volume elements

To model composite materials, a macroscopic composite array and a representative volume element (RVE) must be defined. The two macroscopic periodically-spaced arrays of composite material utilized in this analysis are shown in Figs. 1 and 2. The first macroscopic array is a regular hexagonal array composed of triangular RVEs and the second macroscopic array is a square array composed of square RVEs. The composite arrays each have sides of length w with the interior triangular and square RVEs each having sides of $0.1\,w$. The volume fraction of the composite is 0.33. The fiber diameter was chosen such that the ratio computed by dividing the length of a macroscopic composite edge w by the fiber diameter is approximately equal to 17. The composite arrays can be represented as a periodic assembly of RVEs. The RVE phases are isotropic and linearly elastic and the RVE is assumed to be small compared to the size of the macroscopic composite array. The RVE is not unique with each RVE in the array exhibiting the same deformation to ensure periodicity as
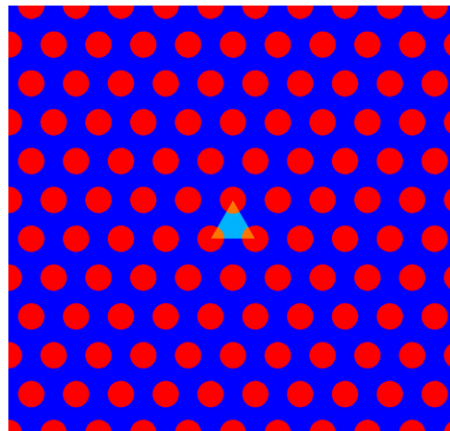

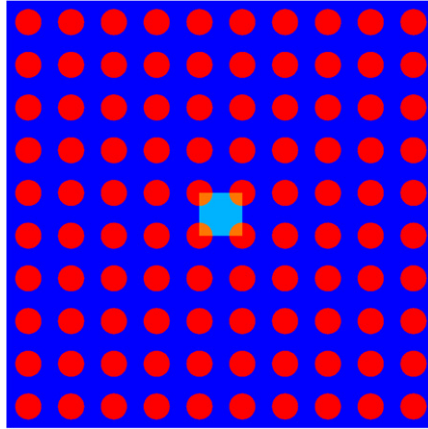Fig. 1. Macroscopic composite array illustrating triangular RVE.

Fig. 2. Macroscopic composite array illustrating square RVE.

the composite array deforms. The average mechanical properties of the entire macroscopic composite array are equal to the average mechanical properties of the RVE.

3. Periodic boundary condition

When analyzing a RVE, periodic boundary conditions must be applied to the RVE to ensure compatibility of deformation and correct computation of stress and strain. A displacement-based finite element method is employed in this analysis. Therefore, the displacements that need to be applied to give a uniform strain field in a corresponding homogeneous composite may be found from the equation:

$$u_i = \epsilon_{ij}^0 x_j \quad i, j = 1, 2, \tag{1}$$

where u_i is the prescribed displacement at some large distance, x_j is a position vector from a reference point to a point on the boundary, and ϵ_{ij}^0 is given by the small-strain tensor according to

$$\epsilon_{ij}^0 = \begin{bmatrix} \epsilon_{11} & \epsilon_{12} \\ \epsilon_{21} & \epsilon_{22} \end{bmatrix}, \tag{2}$$

where ϵ_{ij}^0 is the average strain in the composite array.

Using the node in the lower left corner of the macroscopic composite array as the reference point that remains fixed, a pure shear strain state of

$$\begin{Bmatrix} \epsilon_{11} \\ \epsilon_{22} \\ \epsilon_{12} \end{Bmatrix} = \begin{Bmatrix} 0 \\ 0 \\ 1 \end{Bmatrix} \tag{3}$$

was applied to the arrays shown in Figs. 1 and 2 through the use of Eq. 1. The matrix and fiber properties used in the analysis are those given by Daniel and Ishai (1994) for an E-glass/epoxy composite material. These properties are provided in Table 1. Fig. 3 illustrates the deformation of the triangular and square RVEs of the composite macroscopic array.

Of particular interest is the shape taken by the fiber and matrix regions after deformation. Fig. 3(a) illustrates the deformation of the triangular RVE of the composite macroscopic array shown in Fig. 1 and Fig. 3(b) illustrates the deformation of the square RVE of the composite macroscopic array shown in Fig. 2. It appears that the fiber edges deform linearly and the matrix edges exhibit curvature for each RVE. The linear deformation of the fibers is due to the fact that the stress field inside the inclusion is nearly uniform based on the results of Eshelby (1957) for a single inclusion in an infinite matrix. A uniform stress field gives rise to a linear displacement field. For the matrix edges, Gosz et al. (1992) have concluded that

Table 1
Fiber and matrix properties

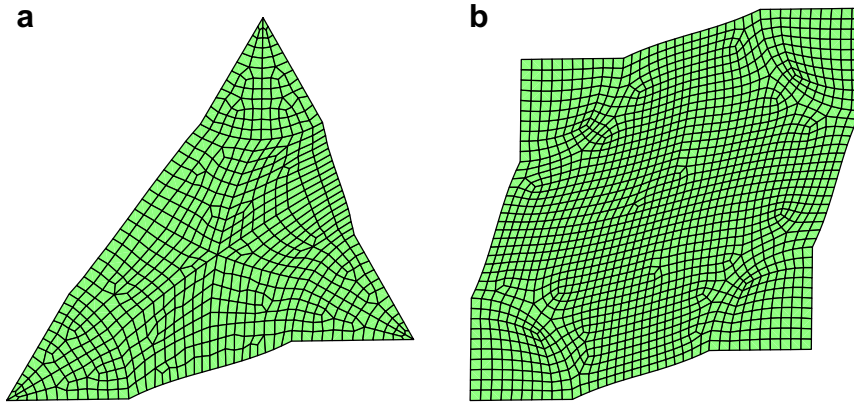| Region	E (GPa)	v
Fiber	69.0	0.20
Matrix	3.45	0.36

Fig. 3. RVE deformation. (a) Triangular composite array. (b) Square composite array.

the displacements must be anti-symmetric about the displacement of the midpoint of an edge of the RVE since each RVE in the model must maintain periodicity and compatibility. To illustrate the argument, consider the adjacent triangular RVEs shown in Fig. 4. Fig. 4(a) illustrates two connected adjacent RVEs in which points P, C, and Q lie on edge AB. The components of the position vector from point A to point P in the unprimed coordinate system are identical to the components of the position vector from point B to point Q in the primed coordinate system. In Fig. 4(b), the adjacent triangles are separated. If the triangle shown in the upper portion of Fig. 4(b) is rotated through 180°, the triangle shown in the lower portion of Fig. 4(b) is obtained. In order to maintain compatibility, the deformation pattern must be the same through the 180° rotation so that the triangles will fit together after deformation. Points A and B', B and A', P and Q', Q and P', and C and C' must share the same space and the displacements must be equal at each pair of points. Therefore, the displacement of point P relative to point A must be equal to the displacement of point Q' relative to point B'; however, the displacement of point Q' relative to point B' must be equal to the displacement of point Q relative to point B after a 180° rotation to ensure the periodicity of the RVE. Hence, we can write

$$\mathbf{d}_P - \mathbf{d}_A = \mathbf{d}_{Q'} - \mathbf{d}_{B'} = -(\mathbf{d}_Q - \mathbf{d}_B) = \mathbf{d}_B - \mathbf{d}_Q, \tag{4}$$

where $\mathbf{d}$ represents the displacement vector. By taking points P and Q to be located at the midpoint of line AB, i.e., coincident with the midpoint C, we can write

$$\mathbf{d}_C - \mathbf{d}_A = \mathbf{d}_B - \mathbf{d}_C \tag{5}$$

for the RVE of Fig. 4(a). Solving Eq. 5 for the displacement at point C yields

$$\mathbf{d}_C = \frac{\mathbf{d}_A + \mathbf{d}_B}{2}. \tag{6}$$

Eq. 6 states that the displacement at the midpoint C must be the average of the displacements at point A and point B since point C is the midpoint of the straight line that connects the two vertices A and B. Thus, it is concluded that the displacements along an edge of the RVE are anti-symmetric about the displacement of the midpoint of the edge of the RVE. The displacement relation given by Eq. 6 must hold for all edges of each RVE in the macroscopic array to maintain compatibility. An odd function remains unchanged after a rotation of 180° and exhibits anti-symmetry. Curve fits performed on the matrix edge displacements indicate that the
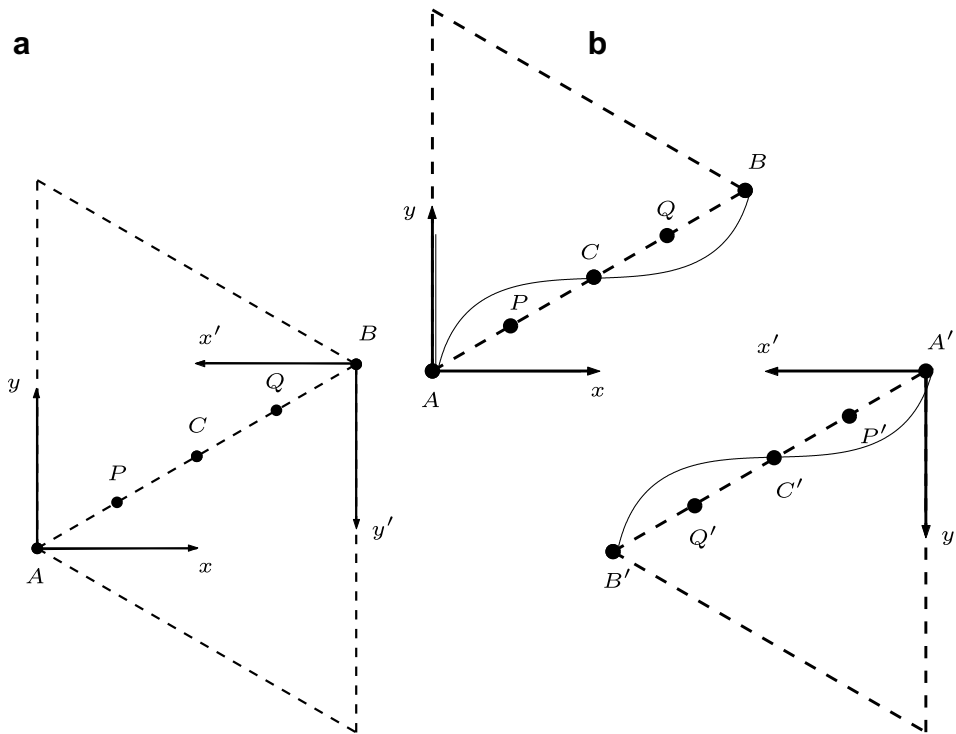
Fig. 4. Adjacent triangular RVEs. (a) Connected RVEs and (b) symmetric deformation.

matrix edge deforms into a cubic shape. Since it is known that the edges of the fibers must deform in a linear fashion and the matrix edges must deform in an anti-symmetric manner, linear interpolants were chosen to model the displacement along the fiber edges and cubic interpolants were chosen to model the displacement along the matrix edges. These interpolants are obtained through the use of shape functions.

4. Shape Functions

Once the nature of the deformed shapes of the fiber and matrix edges is known for the triangular and square RVEs, shape functions can be chosen to interpolate the edge displacements. A cubic interpolant is used to model the displacement along the matrix edges. Dawe (1984) provides the Hermitian shape functions that give rise to the cubic deformation. These shape functions are given below in Eq. 7:

$$
\begin{aligned}
N_1(x) &= 1 - 3\bar{x}^2 + 2\bar{x}^3, \\
N_2(x) &= l(\bar{x} - 2\bar{x}^2 + \bar{x}^3), \\
N_3(x) &= 3\bar{x}^2 - 2\bar{x}^3, \\
N_4(x) &= l(-\bar{x}^2 + \bar{x}^3),
\end{aligned}
\tag{7}
$$

where l is the undeformed length of a matrix edge and $\bar{x} = \frac{x}{l}$, where x is the distance measured along the undeformed matrix edge of length l. The value of $\bar{x}$ is equal to zero at the beginning of a RVE matrix edge and linearly increases along the edge to a maximum value of one at the end of the edge.

A linear interpolant is used along the fiber edges. Linear shape functions are used to characterize these displacements. The linear shape functions used in the analysis are given as:

$$
\begin{aligned}
N_1(x) &= 1 - \bar{x}, \\
N_2(x) &= \bar{x},
\end{aligned}
\tag{8}
$$

where $\bar{x}$ is defined as in Eq. 7, and x is now defined as the distance measured along the undeformed fiber edge of length l.

The shape functions can be used to develop constraint equations that can be implemented on the local level to interpolate the displacements along the fiber and matrix edges. Using this method, each edge of the RVE can be treated individually without depending on node coupling in the finite element mesh. Enforcing the constraint equations in this way along the edges of the RVE reduces the number of unknowns to the interior degrees of freedom of the RVE plus a finite number of global parameters.

5. Constraint equations

Consistent with the finite element method, it is useful to store the cubic shape functions in a matrix called **N**. The displacements of points along a triangle edge can be written in matrix form through the equation

$$\mathbf{u} = \mathbf{Nd}, \tag{9}$$

where **N** is the matrix of shape functions and **d** is a vector of parameters that multiplies the shape functions.

To determine the vector of parameters that is needed to write the cubic constraint equations, it is useful to write the displacements along a RVE matrix edge as

$$u_x(\bar{x}) = d_{1x}N_1 + d_{2x}N_3 + d'_{1x}N_2 + d'_{2x}N_4,$$
$$u_y(\bar{x}) = d_{1y}N_1 + d_{2y}N_3 + d'_{1y}N_2 + d'_{2y}N_4, \tag{10}$$

where u_x and u_y are the displacement components in the horizontal and vertical directions, respectively, the values of d' are the rotations of the RVE matrix edge at its endpoints, and the values of d are equal to the displacements of the end points of each matrix edge. The rotation at the endpoints of a matrix edge defines the rotation of each end of the cubic interpolant and will be defined as θ. The RVE matrix edge displacement equations can therefore be written in matrix notation according to Eq. 9 as

$$\left\{ \begin{matrix} u_x \\ u_y \end{matrix} \right\} = \begin{bmatrix} N_1 & 0 & N_2 & 0 & N_3 & 0 & N_4 & 0 \\ 0 & N_1 & 0 & N_2 & 0 & N_3 & 0 & N_4 \end{bmatrix} \left\{ \begin{matrix} d_{1x} \\ d_{1y} \\ \theta_{1x} \\ \theta_{1y} \\ d_{2x} \\ d_{2y} \\ \theta_{2x} \\ \theta_{2y} \end{matrix} \right\}, \tag{11}$$

where the vector containing the end point displacement values of each RVE matrix edge and the values of the rotation of the cubic interpolant define the parameters needed to completely characterize the cubic displacement along one matrix edge. Insisting that the rotation at each end of the cubic interpolant must be equal for both the horizontal and vertical directions in order to ensure periodicity and compatibility results in the following cubic constraint equations:

$$u_x(\bar{x}) = N_1 d_{1x} + N_3 d_{2x} + (N_2 + N_4)\theta_x,$$
$$u_y(\bar{x}) = N_1 d_{1y} + N_3 d_{2y} + (N_2 + N_4)\theta_y, \tag{12}$$

where θ is the rotation of the cubic interpolant at each end of the matrix edge.

The linear constraint equations are given by

$$u_x(\bar{x}) = N_1 d_{1x} + N_2 d_{2x},$$
$$u_y(\bar{x}) = N_1 d_{1y} + N_2 d_{2y}, \tag{13}$$

where the values of the parameters d are the displacements at each end point of a fiber edge.

6. Local implementation of constraint equations

To demonstrate the local implementation of the constraint equations, consider the simple homogeneous triangular mesh illustrated in Fig. 5. The constraints will be enforced for element 1 in the mesh. The boxed number in the figure indicates the element number and the numbers that are not boxed indicate the local node numbers for the element. The three corner nodes of the triangle, *A*, *B*, and *C*, have fixed prescribed displacements. In order to apply the local implementation of the constraints, the geometry, the element connectivity, and the constrained nodes must first be input into the finite element code by the user to generate a list of constraints that will be used by the finite element code for the local implementation of the boundary conditions.

To generate the constraints, the user must provide the nodal coordinates, the element connectivity list, and the nodes belonging to each fiber or matrix edge of a RVE. The nodes belonging to each fiber or matrix edge of a RVE are stored in node sets with defined end points so that the interpolants can be calculated over each fiber or matrix edge. The end nodes corresponding to each fiber or matrix edge along with the nodal coordinates and connectivity list can then be used to calculate the values of the shape functions at each node along an edge of the RVE. Using the triangular mesh shown in Fig. 5 as an example, three node sets need to be defined to calculate the values of the shape functions. The node sets correspond to the constrained nodes belonging to each edge of the triangle. Once the node sets are defined, the prescribed components of the displacements at the end nodes *A*, *B*, and *C* can be determined since the average strain in the RVE dictates the displacements of the vertices according to

$$
\begin{aligned}
u_i^A &= \epsilon_{ij}^0 x_j^A, \\
u_i^B &= \epsilon_{ij}^0 x_j^B, \\
u_i^C &= \epsilon_{ij}^0 x_j^C,
\end{aligned}
\tag{14}
$$

where the values of u_i are the displacement component values at the vertices, x_j is a position vector from a reference point to a vertex, and ϵ_{ij}^0 is given by Eq. 2. In order to get the correct state of strain in the RVE, the displacement components of the vertices must be given by Eq. 14. In addition to the calculation of the vertex displacements, the shape functions are calculated at the edge nodes defined in the constrained node sets for each element. For each element, the connectivity list is utilized to determine the nodes comprising that element. If a node is to be constrained, the coordinates of the node are determined and the value of $\bar{x}$ is calculated for the fiber or matrix edge to which the node belongs. The value of $\bar{x}$ is then used to calculate the shape function values for the constrained node.
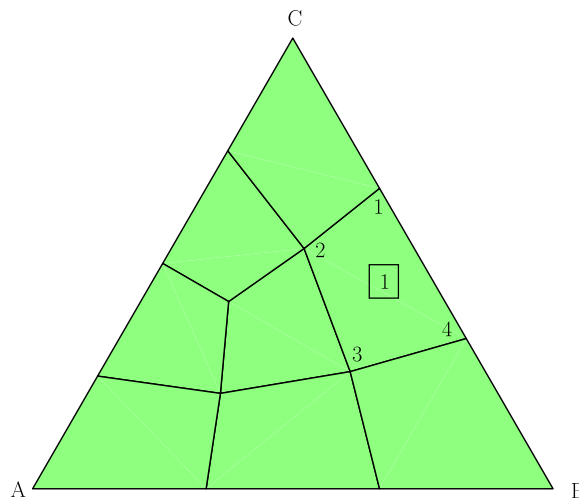

Fig. 5. Simple triangular mesh.

The calculated shape function values are then used to perform the local implementation of the constraints. The nodal coordinates, element connectivity, and material constants need to be input along with the pre-scribed nodal values. The shape function values are provided for the constrained nodes as coefficients multi-plying the end node value of the respective fiber or matrix edge of the RVE according to the definitions of the cubic and linear constraint equations shown in Eqs. 12 and 13. The shape function values are provided for all of the degrees of freedom for each constrained node.

For the constrained degrees of freedom, the linear and cubic shape functions can be stored in a matrix that maps the non-constrained degrees of freedom to the total element degrees of freedom. The mapping between the non-constrained degrees of freedom and the total degrees of freedom for an element can be written as

$$\mathbf{d}_e = \mathbf{L}_e \hat{\mathbf{d}}_e, \tag{15}$$

where $\mathbf{d}_e$ is a vector containing the degrees of freedom for an element, $\mathbf{L}_e$ is a matrix containing the calculated shape functions for the constrained degrees of freedom, and $\hat{\mathbf{d}}_e$ is a vector containing the non-constrained de-grees of freedom for an element. To determine the displacement field throughout the element, the $\mathbf{L}_e$ matrix for the element needs to be set up by first writing

$$
\begin{Bmatrix} d_{1x} \\ d_{1y} \\ d_{2x} \\ d_{2y} \\ d_{3x} \\ d_{3y} \\ d_{4x} \\ d_{4y} \end{Bmatrix}
=
\begin{bmatrix}
1 & 0 & 0 & 0 & 0 & 0 & 0 & 0 \\
0 & 1 & 0 & 0 & 0 & 0 & 0 & 0 \\
0 & 0 & 1 & 0 & 0 & 0 & 0 & 0 \\
0 & 0 & 0 & 1 & 0 & 0 & 0 & 0 \\
0 & 0 & 0 & 0 & 1 & 0 & 0 & 0 \\
0 & 0 & 0 & 0 & 0 & 1 & 0 & 0 \\
0 & 0 & 0 & 0 & 0 & 0 & 1 & 0 \\
0 & 0 & 0 & 0 & 0 & 0 & 0 & 1
\end{bmatrix}
\begin{Bmatrix}
N_1^{(1)} d_{Bx} + N_3^{(1)} d_{Cx} + \left(N_2^{(1)} + N_4^{(1)} \right)\theta_x \\
N_1^{(1)} d_{By} + N_3^{(1)} d_{Cy} + \left(N_2^{(1)} + N_4^{(1)} \right)\theta_y \\
d_{2x} \\
d_{2y} \\
d_{3x} \\
d_{3y} \\
N_1^{(4)} d_{Bx} + N_3^{(4)} d_{Cx} + \left(N_2^{(4)} + N_4^{(4)} \right)\theta_x \\
N_1^{(4)} d_{By} + N_3^{(4)} d_{Cy} + \left(N_2^{(4)} + N_4^{(4)} \right)\theta_y
\end{Bmatrix}, \tag{16}
$$

where the corresponding constraint equations are substituted for the constrained degrees of freedom in the element and the shape functions are evaluated at the constrained degrees of freedom for the element based on the defined constrained fiber and matrix node sets. The superscript number on the shape function values indicates the local node where the shape functions are evaluated for element 1 of Fig. 5. The $\mathbf{L}_e$ matrix can be determined by taking the shape functions out of the vector on the right hand side of Eq. 16 according to

$$
\begin{Bmatrix} d_{1x} \\ d_{1y} \\ d_{2x} \\ d_{2y} \\ d_{3x} \\ d_{3y} \\ d_{4x} \\ d_{4y} \end{Bmatrix}
=
\begin{bmatrix}
0 & 0 & 0 & 0 & N_1^{(1)} & 0 & N_3^{(1)} & 0 & \left(N_2^{(1)} + N_4^{(1)} \right) & 0 \\
0 & 0 & 0 & 0 & 0 & N_1^{(1)} & 0 & N_3^{(1)} & 0 & \left(N_2^{(1)} + N_4^{(1)} \right) \\
1 & 0 & 0 & 0 & 0 & 0 & 0 & 0 & 0 & 0 \\
0 & 1 & 0 & 0 & 0 & 0 & 0 & 0 & 0 & 0 \\
0 & 0 & 1 & 0 & 0 & 0 & 0 & 0 & 0 & 0 \\
0 & 0 & 0 & 1 & 0 & 0 & 0 & 0 & 0 & 0 \\
0 & 0 & 0 & 0 & N_1^{(4)} & 0 & N_3^{(4)} & 0 & \left(N_2^{(4)} + N_4^{(4)} \right) & 0 \\
0 & 0 & 0 & 0 & 0 & N_1^{(4)} & 0 & N_3^{(4)} & 0 & \left(N_2^{(4)} + N_4^{(4)} \right)
\end{bmatrix}
\begin{Bmatrix} d_{2x} \\ d_{2y} \\ d_{3x} \\ d_{3y} \\ d_{Bx} \\ d_{By} \\ d_{Cx} \\ d_{Cy} \\ \theta_x \\ \theta_y \end{Bmatrix}, \tag{17}
$$

where the shape functions are evaluated at the corresponding value of $\bar{x}$ along the respective fiber or matrix edge of the RVE. The values of the shape functions are placed in the appropriate location of the $\mathbf{L}_e$ matrix for an element based on the element's local connectivity list and the constrained node list for each fiber or matrix edge of the RVE. There is a separate $\mathbf{L}_e$ matrix for each element in a mesh. By using the local implementation of the constraints, the number of unknowns has thereby been reduced to the number of interior degrees of

freedom plus two rotation parameters for each edge of the RVE. The unknown degrees of freedom can therefore be solved for through the use of a displacement-based finite element method.

7. Finite element formulation of local constraint implementation

In a displacement-based finite element method, the weak form relating the forces to the displacements through the stiffness matrix results in the following equation for each element:

$$\delta \mathbf{d}_e^{\mathrm{T}}(\mathbf{K}_e \mathbf{d}_e - \mathbf{F}_e) = 0, \tag{18}$$

where $\delta \mathbf{d}_e^{\mathrm{T}}$ is defined to be a vector of arbitrary element virtual displacements, $\mathbf{K}_e$ is the element stiffness matrix, and $\mathbf{F}_e$ is the element force vector. Since the vector of virtual displacements is arbitrary, the quantity inside the parentheses in Eq. 18 must be equal to zero. Hence, the element internal force vector is related to the vector containing the nodal displacements according to

$$\mathbf{F}_e = \mathbf{K}_e \mathbf{d}_e. \tag{19}$$

We are interested in enforcing the constraints on a local level on Eq. 18. From Eq. 15, the virtual displacements can be written as

$$\delta \mathbf{d}_e = \mathbf{L}_e \delta \hat{\mathbf{d}}_e, \tag{20}$$

where $\delta \mathbf{d}_e$ is the vector of virtual displacements and $\delta \hat{\mathbf{d}}_e$ is the vector of non-constrained virtual displacements. Substituting Eqs. 15 and 20 into Eq. 18 results in

$$\left(\delta \hat{\mathbf{d}}_e^{\mathrm{T}} \mathbf{L}_e^{\mathrm{T}} \right) (\mathbf{K}_e \mathbf{L}_e \hat{\mathbf{d}}_e - \mathbf{F}_e) = 0, \tag{21}$$

where $\delta \mathbf{d}_e^{\mathrm{T}}$ is equal to $\delta \hat{\mathbf{d}}_e^{\mathrm{T}} \mathbf{L}_e^{\mathrm{T}}$. Next, the transpose of the matrix $\mathbf{L}_e$ is distributed to result in

$$\left(\delta \hat{\mathbf{d}}_e^{\mathrm{T}} \right) \left(\mathbf{L}_e^{\mathrm{T}} \mathbf{K}_e \mathbf{L}_e \hat{\mathbf{d}}_e - \mathbf{L}_e^{T} \mathbf{F}_e \right) = 0, \tag{22}$$

where $\delta \hat{\mathbf{d}}_e^{\mathrm{T}}$ is a vector of arbitrary non-constrained virtual displacements. Since the virtual displacements are arbitrary, the quantity inside the parentheses of Eq. 22 must be equal to zero, thereby resulting in

$$\mathbf{L}_e^{\mathrm{T}} \mathbf{K}_e \mathbf{L}_e \hat{\mathbf{d}}_e = \mathbf{L}_e^{\mathrm{T}} \mathbf{F}_e. \tag{23}$$

Eq. 23 can now be written as

$$\widehat{\mathbf{K}}_e \hat{\mathbf{d}}_e = \widehat{\mathbf{F}}_e, \tag{24}$$

where

$$\widehat{\mathbf{K}}_e = \mathbf{L}_e^{\mathrm{T}} \mathbf{K}_e \mathbf{L}_e \tag{25}$$

is the modified element stiffness matrix and

$$\widehat{\mathbf{F}}_e = \mathbf{L}_e^{\mathrm{T}} \mathbf{F}_e \tag{26}$$

is the modified element force vector. Eqs. 25 and 26 define the finite element formulation of the local implementation of constraints.

8. Implementation of linear and cubic edge interpolation functions

To implement the local finite element formulation, two sufficiently refined meshes consisting of a triangular RVE and a square RVE were created. The triangular RVE is taken from a periodically-spaced regular hexagonal array of inclusions illustrated in Fig. 1, and the square RVE is taken from a periodically-spaced regular square array of inclusions illustrated in Fig. 2. The results are illustrated for a plane stress analysis. Similar results are obtained for a plane strain analysis. The fiber and matrix properties used in each analysis are those provided in Table 1.

8.1. Triangular unit cell

The first analysis utilizes the triangular RVE. The triangular mesh is composed of 678 four-node quadrilateral elements with a total of 743 nodes. This mesh is shown in Fig. 6. It is desired to demonstrate the local implementation of boundary conditions for a homogeneous material and a composite system using the cubic and linear interpolation functions.

8.1.1. Homogeneous results

The first analysis performed with the triangular unit cell was for a homogeneous material. The mesh was treated as being only composed of matrix material. For the local implementation, the nodal displacements were calculated at the three corner nodes of the triangular RVE shown in Fig. 6 by using Eq. 14 to enforce a desired strain state on the RVE. These nodal displacements were then prescribed at the corners of the triangular RVE and the cubic interpolation functions were used to interpolate the edge displacements for the matrix material composing the entire mesh. The results obtained from the local implementation of the periodic boundary conditions are compared to the response of a RVE within the macroscopic composite. The macroscopic composite was analyzed by using commercial finite element software. In the macroscopic analysis, homogeneous boundary conditions given by Eq. 1 were imposed along the edges of the macroscopic composite array shown in Fig. 1. The strain state utilized for the homogeneous analysis is a state of pure shear given by

$$\epsilon_{ij}^0 = \begin{bmatrix} 0 & 1 \\ 1 & 0 \end{bmatrix}, \tag{27}$$

where ϵ_{ij}^0 is the average strain in the composite. Fig. 7 illustrates that the displacements obtained from applying homogeneous displacement boundary conditions on the boundary of the macroscopic cell shown in Fig. 1 are the same as imposing the constraints locally on the triangular RVE shown in Fig. 6. It is important to note that the mesh of the macroscopic representative cell in Fig. 1 is composed of a periodic arrangement of the triangular mesh shown in Fig. 6, so the triangular mesh at the center of Fig. 1 is identical to the mesh of Fig. 6. The cubic constraint equations without the presence of fiber material result in edges that are linear for the matrix material. Tables 2 and 3 illustrate the results of the average stress and strain obtained in the triangular RVE for the case of pure shear. Note that all average stress and strain results were calculated from the stresses and strains obtained at the quadrature points. Good agreement is seen between the values obtained from the local and macroscopic implementations, with a very small percent difference of 0.08%. Also note that the strain state imposed on the large cell of Fig. 1 shown in Eq. 27 is obtained as the average strain in the triangular RVE in both the local and macroscopic cases.

After the homogeneous analysis, fibers of equal radii were added to the mesh as shown in Fig. 8 in order to perform the analysis on the triangular unit cell of the two-dimensional hexagonal array composite system. The properties provided in Table 1 were used for the corresponding fiber and matrix sections of the mesh.
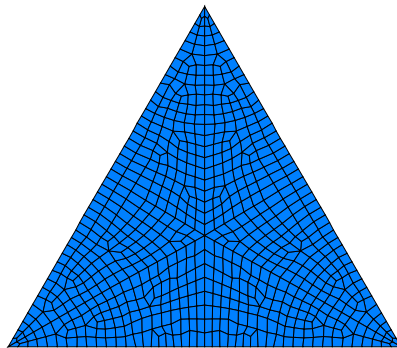

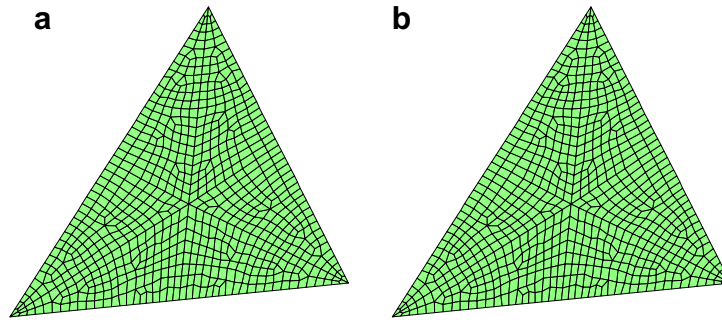Fig. 6. Homogeneous triangle RVE mesh.

Fig. 7. Displacement results for pure shear on homogeneous mesh. (a) Macroscopic RVE and (b) local implementation.

Table 2
Average stress results for homogeneous RVE (GPa)

Strain state	Implementation	$\overline{\sigma}_{11}$	$\overline{\sigma}_{22}$	$\overline{\sigma}_{12}$
Pure shear	Macroscopic	−0.00223	−0.00134	2.535
Pure shear	Local	0	0	2.537

Table 3
Average strain results for homogeneous RVE

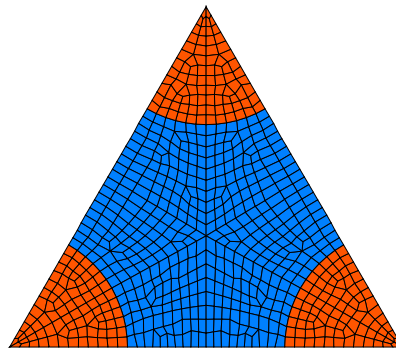| Strain state	Implementation	$\overline{\epsilon}_{11}$	$\overline{\epsilon}_{22}$	$\overline{\epsilon}_{12}$
Pure shear	Macroscopic	0	0	0.999
Pure shear	Local	0	0	1.000

Fig. 8. Triangular RVE with fibers added.

Comparison of the results of imposing the periodic boundary conditions at the macroscopic versus local level for the strain states of pure shear, pure tension, and a combined state consisting of shear and tension were performed for the composite mesh.

8.1.2. Results for pure shear

The strain state utilized for pure shear is given in terms of Eq. 2 as

$$\epsilon_{ij}^0 = \begin{bmatrix} 0 & 1 \\ 1 & 0 \end{bmatrix}, \tag{28}$$

where ϵ_{ij}^0 is the average strain in the composite. The local implementation of the boundary conditions was performed on the triangular RVE shown in Fig. 8. The three corner nodal displacements were calculated by using
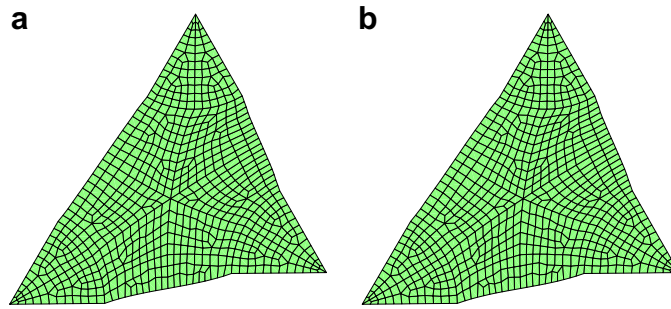
Fig. 9. Displacement results for pure shear. (a) Macroscopic RVE and (b) local implementation.

Eq. 14 to enforce the desired strain state on the RVE. Once the three corner nodal displacements were prescribed, the cubic constraint equations were enforced for the matrix material and the linear constraint equations were enforced for the fiber material. The displacement results for the triangular RVE are shown in Fig. 9 for both the macroscopic and local implementations of the periodic boundary conditions. The figure illustrates that the displacements obtained in both cases exhibit excellent agreement. The displacements were determined to match for both cases to three significant figures. Fig. 9 clearly illustrates the cubic shape of the edges of the matrix material and the linear edges of the fiber material.

Plots of von Mises stress in the triangular RVE for the case of pure shear appear in Fig. 10. The von Mises effective stress is given as

$$\sigma_e = \sqrt{3J_2}, \tag{29}$$

where

$$J_2 = \frac{1}{2}S_{ij}S_{ij}, \tag{30}$$

and

$$S_{ij} = \sigma_{ij} - \frac{1}{3}\sigma_{kk}\delta_{ij}, \tag{31}$$

where S_{ij} are the deviatoric stress components obtained by subtracting the mean stress from the Cauchy stress components, δ_{ij} is the Kronecker delta, σ_e is the von Mises effective stress, and the subscripts i and j range from 1 to 3. Table 4 contains the average stress and maximum von Mises stress results, and Table 5 contains the average strain results obtained for both the macroscopic and local implementations of the periodic boundary conditions for pure shear.
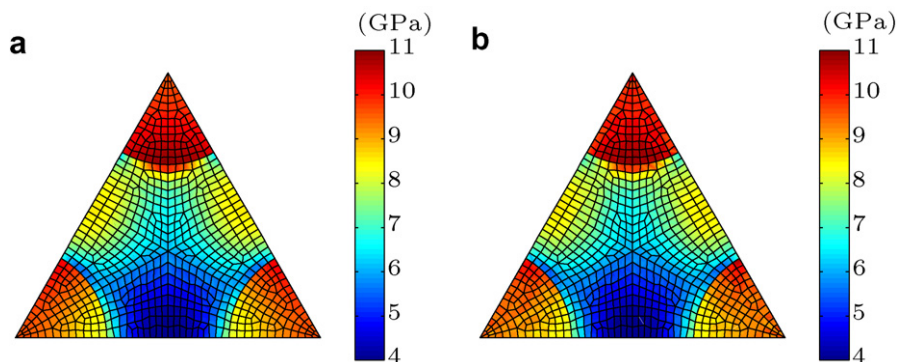

Fig. 10. Von Mises stress results for pure shear. (a) Macroscopic RVE and (b) local implementation.

Table 4
Stress results for triangular RVE (GPa)

Strain state	Implementation	$\overline{\sigma}_{11}$	$\overline{\sigma}_{22}$	$\overline{\sigma}_{12}$	$\sigma_{\mathrm{vm}}^{\max}$
Pure shear	Macroscopic	−0.00238	−0.00162	4.276	11.080
Pure shear	Local	0	0	4.249	11.020
Tension	Macroscopic	6.484	2.228	−0.0099	8.092
Tension	Local	6.492	2.245	0	8.102
Combined state	Macroscopic	5.474	7.604	4.269	14.240
Combined state	Local	5.491	7.617	4.249	14.681

Table 5
Average strain results for triangular RVE

Strain state	Implementation	$\overline{\epsilon}_{11}$	$\overline{\epsilon}_{22}$	$\overline{\epsilon}_{12}$
Pure shear	Macroscopic	0	0	1.001
Pure shear	Local	0	0	1.000
Tension	Macroscopic	1.000	−0.00263	−0.00233
Tension	Local	1.000	0	0
Combined state	Macroscopic	0.498	0.999	1.005
Combined state	Local	0.500	1.000	1.000

8.1.3. Results for tension

The strain state utilized for tension is given in terms of Eq. 2 as

$$\epsilon_{ij}^0 = \begin{bmatrix} 1 & 0 \\ 0 & 0 \end{bmatrix}, \tag{32}$$

where ϵ_{ij}^0 is the average strain in the composite. This strain state represents a one-dimensional extensional straining of the solid. The displacement results obtained from applying homogeneous displacement boundary conditions on the boundary of the macroscopic composite and the results obtained from the local implementation are shown in Fig. 11. The von Mises stress results plotted in Fig. 12 for tension exhibit excellent agreement between the macroscopic and local implementations of the periodic boundary conditions. Table 4 contains stress and maximum von Mises stress results, and Table 5 contains the average strain results obtained for both the macroscopic and local implementations of the periodic boundary conditions for tension.

8.1.4. Results for combined strain state

The strain state utilized for the combined strain state is given in terms of Eq. 2 as

$$\epsilon_{ij}^0 = \begin{bmatrix} 0.5 & 1 \\ 1 & 1 \end{bmatrix}, \tag{33}$$

where ϵ_{ij}^0 is the average strain in the composite. The displacement results obtained from applying homogeneous displacement boundary conditions on the boundary of the macroscopic composite and the results
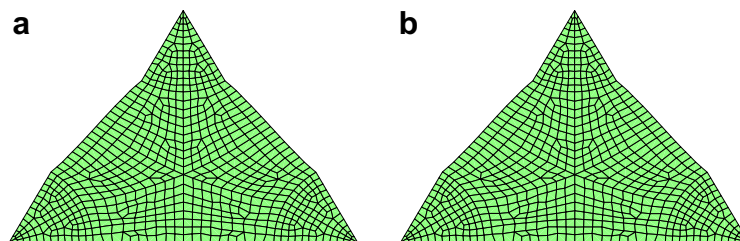

Fig. 11. Displacement results for tension. (a) Macroscopic RVE and (b) local implementation.
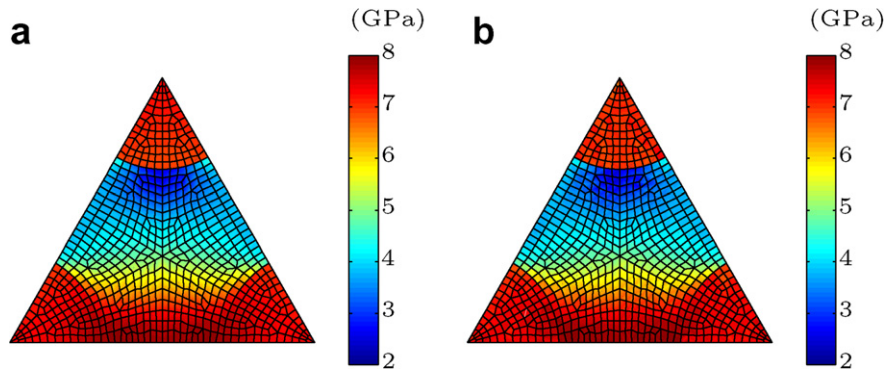
Fig. 12. Von Mises stress results for tension. (a) Macroscopic RVE and (b) local implementation.
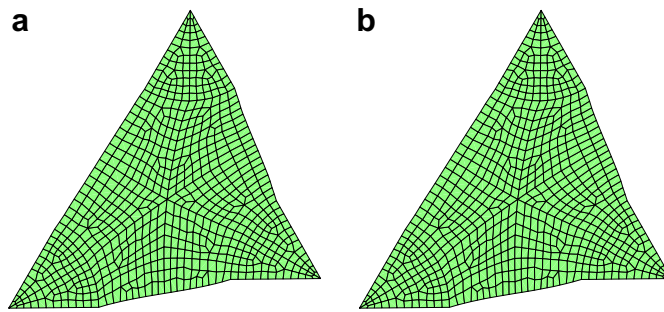

Fig. 13. Displacement results for combined strain state. (a) Macroscopic RVE and (b) local implementation.
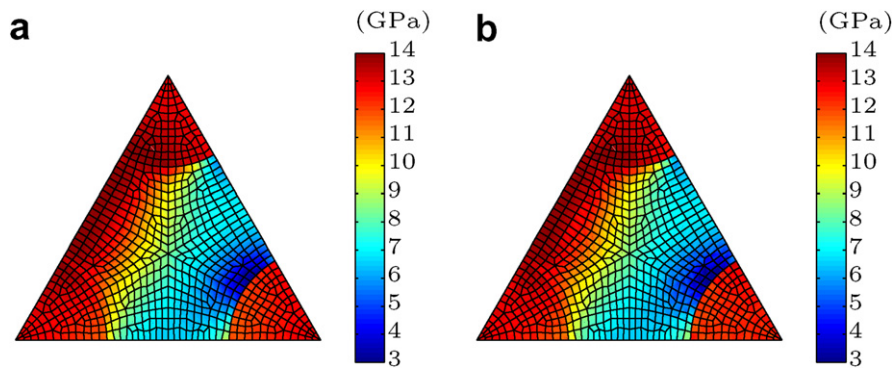

Fig. 14. Von Mises stress results for combined strain state. (a) Macroscopic RVE and (b) local implementation.

obtained from the local implementation are shown in Fig. 13. The von Mises stress results plotted in Fig. 14 for the combined strain state again exhibit excellent agreement between the macroscopic and local implementations of the periodic boundary conditions. Table 4 contains the average stress and maximum von Mises stress results, and Table 5 contains the average strain results obtained for both the macroscopic and local implementations of the periodic boundary conditions for the combined strain state.

8.2. Square unit cell

After the analysis using the triangular RVE, it was desired to illustrate the method's application to other geometries as well as show the method's application to non-periodic meshes. To illustrate the implementation, consider the two meshes shown in Fig. 15. The mesh illustrated in Fig. 15(a) is a periodic mesh of a square
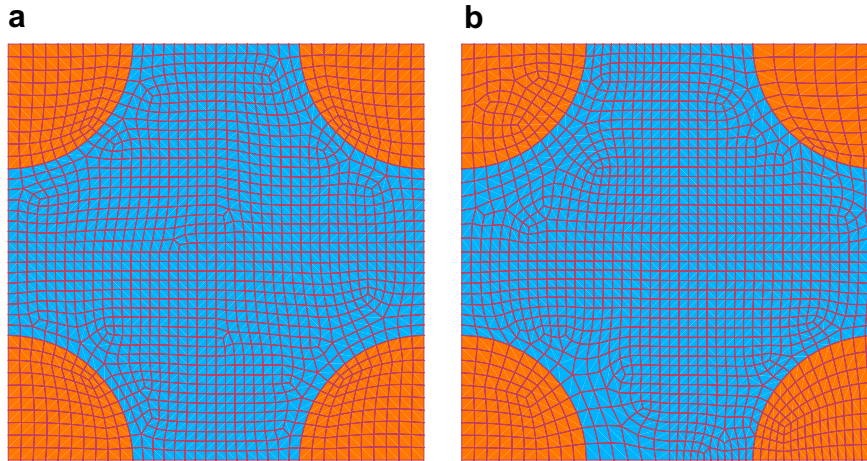
a   **b**

Fig. 15. Mesh designs of square RVE. (a) Periodic mesh and (b) non-periodic mesh.

RVE consisting of 1638 four-node quadrilateral elements, and the mesh illustrated in Fig. 15(b) is a non-periodic mesh consisting of 1605 four-node quadrilateral elements. Notice that the periodic mesh in Fig. 15(a) contains equal numbers of paired nodes and elements on opposite fiber and matrix edges of the mesh, while the mesh in Fig. 15(b) does not. Using a conventional node-coupling scheme would require an equal number of paired nodes on opposite fiber and matrix edges of the mesh in order to enforce constraint equations to ensure periodicity and compatibility. It is desired to compare the results of the local implementation of the constraints on each mesh with the results of enforcing the constraints on the macroscopic composite shown in Fig. 2, which is composed of a periodic arrangement of the periodic mesh illustrated in Fig. 15(a).

To begin the analysis, a strain state of pure shear,

$$\epsilon_{ij}^0 = \begin{bmatrix} 0 & 1 \\ 1 & 0 \end{bmatrix},$$ (34)

was applied to the square RVE shown in Fig. 15(a) through the use of Eq. 14 and the corner displacements of the square RVE were obtained. These displacements were then prescribed at the corners of each square RVE shown in Fig. 15 and the cubic and linear interpolants were used to enforce the local implementation of the constraints on the periodic and non-periodic meshes. The displacement results with the von Mises stress results superimposed on the meshes are illustrated in Fig. 16(a) for the periodic square mesh and Fig. 16(b) for the
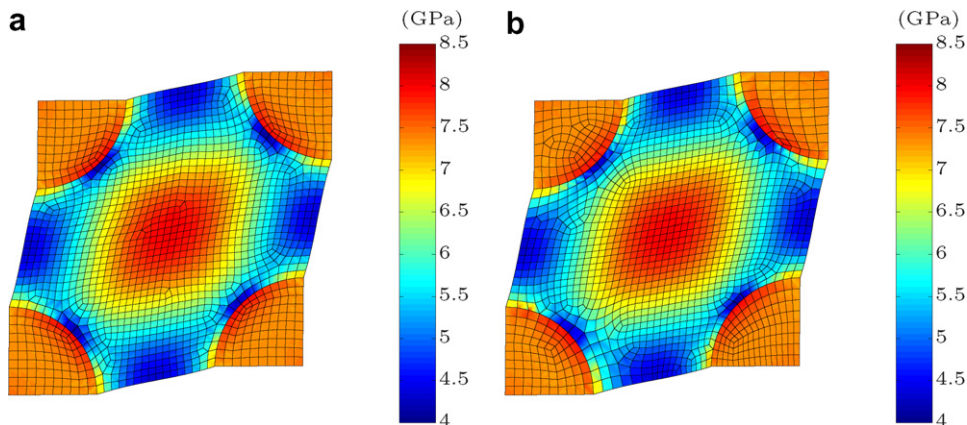
a   (GPa)   **b**   (GPa)

Fig. 16. Results of local implementation of constraints on square RVE. (a) Periodic mesh and (b) non-periodic mesh.

Table 6
Stress results for square meshes in pure shear (GPa)

Mesh	Implementation	$\bar{\sigma}_{11}$	$\bar{\sigma}_{22}$	$\bar{\sigma}_{12}$	σ_{vm}^{max}
Periodic	Macroscopic	0	0	3.700	8.249
Periodic	Local	0	0	3.691	8.067
Non-periodic	Local	0	0	3.691	8.327

Table 7
Average strain results for square meshes in pure shear

Mesh	Implementation	$\bar{\epsilon}_{11}$	$\bar{\epsilon}_{22}$	$\bar{\epsilon}_{12}$
Periodic	Macroscopic	0	0	1.003
Periodic	Local	0	0	1.000
Non-periodic	Local	0	0	1.000

non-periodic square mesh. Tables 6 and 7 contain the average values of stress and strain along with the maximum values of von Mises stress obtained for the periodic and non-periodic meshes for both the macroscopic and local implementations of the constraints. Once again, excellent agreement among the results was obtained. Note that the strain state of pure shear imposed on the macroscopic composite array is again obtained as the average strain in the RVE for all three cases.

9. Conclusion

A local approach of imposing displacement-based boundary conditions for composite materials has been demonstrated through the use of the finite element method. The local approach is carried out by utilizing a cubic interpolant to model the displacement field along the matrix edges and a linear interpolant to model the field along the fiber edges. The results of the local implementation match the results obtained by applying homogeneous boundary conditions to a macroscopic composite. A key advantage of the local implementation of periodic boundary conditions for the micromechanical modeling of fiber composite materials when compared to a conventional node-coupling scheme is the ability to model large representative volume elements without enforcing a large number of constraint equations. To apply the boundary conditions using a conventional node coupling scheme, potentially thousands of constraint equations need to be enforced to impose constraints on opposite nodes of the mesh. Computation of a large number of nodes can be a very time-consuming task. With the local implementation, displacements based on the desired strain state in the RVE simply need to be calculated and prescribed at the corner nodes of an RVE and the number of unknowns thereby reduces to the interior degrees of freedom plus two global rotation parameters for each edge of the RVE while using the interpolation functions to determine the edge displacements of the RVE. This reduction can drastically reduce the computational resources needed to enforce the constraints and determine all of the unknowns in a large mesh. It has also been demonstrated that the method is applicable to non-periodic meshes that do not exhibit equal numbers of nodes on opposite edges as is required with the existing implementations of periodic boundary conditions, thereby allowing flexibility in mesh creation. The demonstrated local implementation of periodic boundary conditions does not require a periodic mesh. Only the inclusion intersections with the RVE edges must be periodic, i.e., if a particle intersects the RVE edge, the part of the particle that extends beyond the RVE edge must reappear at the corresponding edge of the RVE. The meshing of the RVE itself does not have to be periodic, thereby allowing the use of more generic mesh generation. In addition, the mesh of the RVE is not limited to constant strain elements.

The benefits of the local implementation of boundary conditions are expected to be fully realized in a three-dimensional model since the surfaces of such meshes contain a large number of nodes. Before extending the method to three dimensions, the types of surfaces expected on the outer faces of the RVE will need to be established. For example, three-dimensional surfaces such as plane surfaces on the fibers and cubic splines on the

matrix may be able to be used in a three-dimensional formulation. The three-dimensional implementation is a study to be performed in future work on composite micromechanical modeling.

References

Berger, H., Kari, S., Gabbert, U., Rodriguez-Ramos, R., Guinovart, R., Otero, J., Bravo-Castillero, J., 2005. An analytical and numerical approach for calculating effective material coefficients of piezoelectric fiber composites. International Journal of Solids and Structures 42, 5692–5714.

Bianchi, S., Corigliano, A., Frassine, R., Rink, M., 2006. Modelling of interlaminar fracture processes in composites using interface elements. Composites Science and Technology 66, 255–263.

Christensen, R., 1990. A critical evaluation for a class of micromechanics models. Journal of the Mechanics and Physics of Solids 38, 379–404.

Corigliano, A., 1993. Formulation, identification, and use of interface models in the numerical analysis of composite delamination. International Journal of Solids and Structures 30, 2779–2811.

Daniel, I., Ishai, O., 1994. Engineering Mechanics of Composite Materials. Oxford University Press, New York, New York.

Dawe, D., 1984. Matrix and finite element displacement analysis of structures. Oxford University Press, New York, New York.

Drugan, W., Willis, J., 1996. A micromechanics-based nonlocal constitutive equation and estimates of representative volume element size for elastic composites. Journal of the Mechanics and Physics of Solids 44, 497–524.

Eckschlager, A., Han, W., Bohm, H., 2002. A unit cell model for brittle fracture of particles embedded in a ductile matrix. Computational Materials Science 25, 85–91.

Eshelby, J., 1957. The determination of the elastic field of an ellipsoidal inclusion, and related problems. Proceedings of the Royal Society of London A 241, 376–396.

Gosz, M., Moran, B., Achenbach, J., 1991. Effect of a viscoelastic interface on the transverse behavior of fiber-reinforced composites. International Journal of Solids and Structures 27, 1757–1771.

Gosz, M., Moran, B., Achenbach, J., 1992. Load-dependent constitutive response of fiber composites with compliant interphases. Journal of the Mechanics and Physics of Solids 40, 1789–1803.

Gusev, A., 1997. Representative volume element size for elastic composites: A numerical study. Journal of the Mechanics and Physics of Solids 45, 1449–1459.

Gusev, A., 2001. Numerical identification of the potential of whisker- and platelet-filled polymers. Macromolecules 34, 3081–3093.

Hashin, Z., 1983. Analysis of composite materials – A survey. Journal of Applied Mechanics 50, 481–505.

Hashin, Z., 1992. Extremum principles for elastic heterogenous media with imperfect interfaces and their application to bounding of effective moduli. Journal of the Mechanics and Physics of Solids 40, 767–781.

Hashin, Z., Shtrikman, S., 1963. A variational approach to the theory of the elastic behaviour of multiphase materials. Journal of the Mechanics and Physics of Solids 11, 127–140.

Liu, H., Mai, Y., 1999. An appraisal of composite interface mechanics models and some challenging problems. Composite Interfaces 6, 343–362.

Llorca, J., Segurado, J., 2004. Three-dimensional multiparticle cell simulations of deformation and damage in sphere-reinforced composites. Materials Science and Engineering A 365, 267–274.

Needleman, A., 1987. A continuum model for void nucleation by inclusion debonding. Journal of Applied Mechanics 54, 525–531.

Schellekens, J., DeBorst, R., 1993. On the numerical integration of interface elements. International Journal for Numerical Methods in Engineering 36, 43–66.

Segurado, J., Llorca, J., 2002. A numerical approximation to the elastic properties of sphere-reinforced composites. Journal of the Mechanics and Physics of Solids 50, 2107–2121.

Segurado, J., Llorca, J., 2004. A new three-dimensional interface finite element to simulate fracture in composites. International Journal of Solids and Structures 41, 2977–2993.

Thoutireddy, P., Molinari, J., Repetto, E., Ortiz, M., 2002. Tetrahedral composite finite elements. International Journal for Numerical Methods in Engineering 53, 1337–1351.

Tsai, S., Hahn, H., 1980. Role of interface in the strength of composite materials. Polymer Science and Technology 12, 463–472.

Yeh, J., 1992. The effect of interface on the transverse properties of composites. International Journal of Solids and Structures 29, 2493–2502.